Applied Materials Today 46 (2025) 102890

Contents lists available at ScienceDirect

Applied Materials Today

journal homepage: www.elsevier.com/locate/apmt

Investigation of structure, optical properties and chemical stability of the KL1421 pyridinium luminophore with high quantum yield

Viktor Zabolotnii [a], Jelena Tamuliene [b], Matiss Martins Drava [c,d], Teodora Kirova [a], Iryna Tepliakova [a], Vanesa Lukinsone [a], Artis Kinens [c,d,*], Roman Viter [a,*]

[a] Faculty of Exact Sciences and Technologies, University of Latvia, Jelgavas street 3, Riga, LV 1004, Latvia
[b] Institute of Theoretical Physics and Astronomy, Vilnius University, Saulėtekio av. 3, Vilnius 10257, Lithuania
[c] Faculty of Medicine and life Sciences, University of Latvia, Jelgavas street 1, Riga, LV 1004, Lativa
[d] Latvian Institute of Organic Synthesis, Aizkraukles street 21, Riga, LV 1006, Latvia

ARTICLE INFO

Keywords:
Organic luminophore
Photoluminescence
Optical sensor
Chemical stability
Adsorption

ABSTRACT

This study reports on the synthesis sturcutre and optical properties of a novel pyridinium luminophore (KL1421). The main properties of the KL1421 have been modeled by quantum chemistry calculations using the B3LYP method. The structure, electronic, and optical properties of the KL1421 have been investigated by ^{1}H NMR, FT-IR, XRD, diffuse reflectance, and photoluminescence spectroscopy. The stability of the optical signal and application of the KL1421 as a gas sensor for the detection of water, ammonia, and acetic acid vapors were evaluated.

Analysis of theoretical and experimental results exhibits a significant difference in the KL1421 optical properties due to limitations of the selected calculation model. Theoretical calculations have predicted a weak interaction between KL1421 and adsorbed water and ammonia molecules. No chemical interactions and phase transitions have been foreseen by calculations in the interaction between KL1421 and acetic acid.

Experimental results showed non-covalent interaction and phase transitions after exposure to water and ammonia environment, and acetic acid, respectively. Weak interaction and crystallinity changes were observed by ^{1}H NMR, XRD, FTIR, and UV-Vis absorption spectra. Red shift of the absorption edge was found after interaction with target molecules, explained by the change of the HOMO-LUMO transition energy.

Analysis of interaction by photoluminescence spectroscopy showed high quantum yield (QY) for the KL1421 (80 %) and high stability of the signal with low noise to signal ratio (3 %).

Adsorption of the target molecules was irreversible, remaining physisorbed molecules onto KL1421 surface. It led to insignificant changes of QY (77-78 %) and slight red shift of photoluminescence peak position after exposure to water and ammonia. Strong interaction with acetic acid led to a decrease of the QY to 35 %, red shift of the emission peak position, and decrease of the photoluminescence intensity (60 %). Analysis of the structure and optical properties enables to propose mechanism of interaction between KL1421 and acetic acid, based on hydrogen bonding to the mesylate ion. The formation of new complexes induced phase transitions and changes in charge transfer mechanisms. We propose dual-mode measurements, based on photoluminescence and diffuse reflectance, to evaluate the strength of the interaction between KL1421 and volatile molecules.

At this stage, the developed KL1421 luminophores didn't show good sensitivity towards the selected target molecules. They show good potential as photoluminescent markers for emerging applications in environments with high humidity and pH. Improvement of sensor properties requires modification of the chemical structure and investigation of sensitivity towards other volatile acids.

1. Introduction

Pyridinium luminophores (PyL) are a new class of organic materials that demonstrate high quantum yield and tunable emission in the visible range [1–3]. Typically, the organic luminophores can be divided into two broad categories: ones containing neutral π systems [4], such as

---

[*] Corresponding authors.
E-mail addresses: artis.kinens@lu.lv (A. Kinens), roman.viter@lu.lv (R. Viter).

https://doi.org/10.1016/j.apmt.2025.102890
Received 13 April 2025; Received in revised form 22 July 2025; Accepted 8 August 2025

phenyl or naphthyl rings, and ones containing charged π^+ heteroaromatic systems, such as imidazolium or pyridinium (Py^+) cations [5, 6]. Both systems exhibit different behavior in aggregates. For example, luminophores containing only π systems are highly efficient in solutions; however, they are non-luminescent in solid states such as thin polymer films or crystals, thus exhibiting aggregation-caused quenching (ACQ) [7]. The formation of both intermolecular π–π^+ [8] and π^+–π^+ interactions [5,6,9,10] have been associated with strong emission of the Py^+ salts in the solid states. It was demonstrated that the efficiency of the emission of cationic solid-state luminophores is directly proportional to the intermolecular charge transfer intensity [11]. Furthermore, the π^+–π^+ interactions contributed up to 96 % of the electronic coupling between luminophores in the crystal lattice. Therefore, the design and tailoring of intermolecular charge transfer and π^+–π^+ interactions will define the optical properties of the Py^+ salts in the solid state.

Due to these properties, these materials have been actively used as materials for light screens [2], light-emitting applications [12], chemical sensors [12,13], and biosensors [3]. The emission stability in emerge atmospheres (highly acidic, highly basic, and high humidity) is a new challenging area of environmental applications of organic luminophores [14–17]. Photoluminescence stability of organic luminophores is an important parameter for space, industrial, and monitoring applications where organic luminophores could be used as functional coating or sensing element [15,17,18]. Based on the recent publications, the studies of the chemical stability of the PyL optical properties in emergent atmospheres have not been explored yet.

Optical sensors for the detection of volatile organic compounds are a new developing research field [15]. Absorbance, reflectance, and photoluminescence spectroscopy are typically used as detection methods [15]. Opposite to classical metal oxide resistive gas sensors, the optical sensors work at room temperature and don't require any special technologies (lithography for contact fabrication, thick/thin film processing, etc.) for sample preparation [15]. In our previous works, we have reported on ZnO-based photoluminescence gas sensors for the detection of ethanol and acetic acid [19]. The as-prepared and polymer-modified photoluminescent ZnO nanostructures have been used as sensor elements [20] and optical transducers [19], respectively. Due to interaction between the sensor surface and target molecules, the changes in photoluminescence spectra have been recorded, and a calibration curve vs concentration of the target molecules has been obtained [19]. Photoluminescence of TiO_2 nanostructures has been used for the detection of gases and volatile compounds. The developed sensors showed good sensitivity and selectivity to the target molecules [21–23].

The metal oxide-based optical sensors had one disadvantage as low quantum yield. It requires a high-power excitation source to initiate emission and expensive equipment (photomultipliers and spectrometers) to measure it [21]. New PyL materials with high quantum yield and good sensitive properties could replace metal oxide-based materials in such applications [24,25].

Prediction of the interaction between the surface of luminophore and adsorbed molecules is an important key factor in material design, fabrication, and application [14,25]. Quantum chemistry methods, such as B3LYP, PBE0, M06-2X, and ωB97X [26–28] allow for calculating interaction mechanisms between the adsorbed molecules and the luminophore and predict changes of the main properties of the luminophore, such as chemical structure, FTIR, Raman, absorbance, and photoluminescence. This allows tuning of the luminophore's stability, sensor response, selectivity, and mechanisms of interaction with target molecules. To our knowledge, quantum chemistry calculations and investigation of the interaction between PyL and gas molecules have not been performed yet.

In this paper, we present a theoretical and experimental investigation of the structure, optical, and sensor properties of KL1421 luminophore originally designed by Leduskrasts et al [11]. Fundamental properties of the luminophores were modeled by quantum chemistry methods. HOMO and LUMO analysis, structure geometry, and absorption spectra were calculated before and after interaction with selected volatile model molecules which are capable of forming non-covalent interactions and exhibiting varied pH characteristics such as water (H_2O), ammonia (NH_3), and acetic acid (AcOH). The structure, optical, and sensitive properties of the luminophores were studied by ^{1}H NMR, XRD, FTIR, diffuse reflectance, and photoluminescence spectroscopy. Interaction between the KL1421 luminophore and target molecules has been discussed. The obtained theoretical and experimental results have been compared. Similarities and deviations between theoretical and experimental results have been explained. Future prospects of the novel pyridinium luminophores for applications in gas sensors and functional coatings have been described.

2. Experimental part

2.1. Synthesis

Synthesis of luminophore KL1421 was performed by following the experimental procedure reported by Leduskrasts et al. (see Fig 1) [11]. The ^{1}H-NMR spectra of obtained compounds correspond to those reported in the literature [11]. The solvents and reagents used were purchased from commercial sources - *Acros Organics, Sigma-Aldrich, Alfa Aesar, Fisher Chemical*, and *Fluorochem* - and used without additional purification. The reaction progress was monitored using LC-MS system consisting of *Waters Alliance 2695* system and *Waters Alliance 2996* photodiode detector, using a *Waters Bridge Xbridge* C18 3.5 µm, 2.1 mm, 50 mm column with 0.5 mL/min flow rate. The gradient eluent from 90:10 of 0.01 % TFA aqueous solution/MeCN to 5:95 of 0.01 % TFA aqueous solution/MeCN was used for analysis.

The obtained compound's ^{1}H NMR spectra were recorded in $CDCl_3$ and MeOD-d_4 solutions using a Bruker Fourier-300 spectrometer. For the ^{1}H NMR spectrum, the non-deuterated residual signals of $CDCl_3$ (7.26 ppm) and MeOD-d_4 (3.31 ppm) were used as internal standards. Chemical shifts are reported in the δ scale and J constants were measured in hertz (Hz). Multiplicities are indicated with the symbols: s (singlet), d (doublet), t (triplet), q (quartet), and m (multiplet).

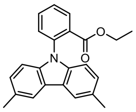

Ethyl 2-(3,6-dimethyl-9H-carbazol-9-yl)benzoate (**3**). Carbazole **1** (0.40 g, 2.00 mmol, 1.0 equiv.), K_2CO_3 (1.00 g, 7,70 mmol, 3.9 equiv.) and *L*-proline (88.0 mg, 0.80 mmol, 0.4 equiv.) were loaded in a 25 mL pressure vial. The vial was dried under vacuum for 10 min at 60°C. Then CuI (120 mg, 0.60 mmol, 0.3 equiv.) was added and the vial was purged with argon and sealed. Then ethyl 2-bromobenzoate (**2**) (0.80 ml, 5.00 mmol, 2.5 equiv.) was added, followed by anhydrous DMSO (9 mL). The argon was bubbled through the blue suspension for 10 min and then heated at 145°C for 48 h. After cooling, the brown suspension was diluted with water (50 mL) and extracted with DCM (4 × 70 mL). The combined organic layers were dried over anhydrous Na_2SO_4 and purified by *flash* column chromatography (SNAP 60 g C18 column, 40 mL/min flow rate, gradient from 75 % H_2O to 100 % MeCN, over 12 CV). Fractions containing product **3** were combined and purified by *flash* column chromatography (100 g SiO_2 column, 30 mL/min flow rate, from 2 % EtOAc to 91 % petroleum ether) to obtain **3** as a colorless viscous oil (0.57 g, 85 %); analytical TLC on silica gel, 1:10 EtOAc/petroleum ether, R_f =0.40.

^{1}H NMR (300 MHz, $CDCl_3$) δ 8.14 – 8.06 (m, 1H), 7.90 – 7.85 (m, 2H), 7.76 – 7.69 (m, 1H), 7.61 – 7.52 (m, 2H), 7.20 – 7.13 (m, 2H), 7.03 – 6.97 (m, 2H), 3.68 (q, J = 7.1 Hz, 2H), 2.53 (s, 6H), 0.44 (t, J = 7.1 Hz, 3H).

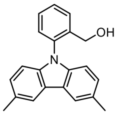

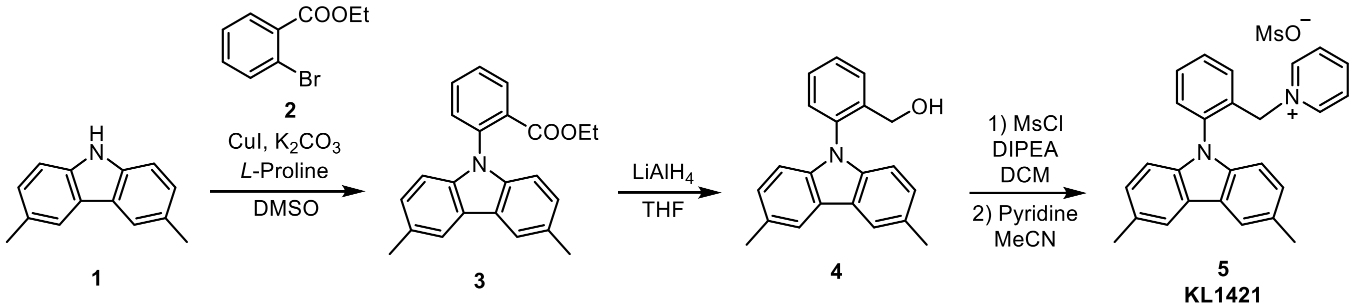

Fig. 1. Synthesis scheme of luminophore KL1421 [11].

(2-(3,6-Dimethyl-9H-carbazol-9-yl)phenyl)methanol (**4**). Anhydrous THF (10 mL) solution of ethyl 2-(3,6-dimethyl-9H-carbazol-9-yl) benzoate (**3**) (0.54 g, 1.60 mmol, 1.0 equiv.) was dropwise added to a $LiAlH_4$ solution (4M, 1.00 mL, 4.00 mmol, 2.5 equiv) in diethyl ether at 0°C. The white suspension was stirred at room temperature for 1 h. Then cooled in an ice bath and quenched in a sequence by dropwise addition of water (0.15 mL), aqueous 4M NaOH solution (0.30 mL), and water (0.45 mL). The obtained white suspension was filtered through a pad of ceilte, washed with THF, and evaporated to yield product **4** as a viscous colorless oil (0.47 g, 98 %).

^{1}**H NMR** (300 MHz, $CDCl_3$) δ 7.96 – 7.88 (m, 2H), 7.81 – 7.73 (m, 1H), 7.62 – 7.46 (m, 2H), 7.40 – 7.32 (m, 1H), 7.23 – 7.15 (m, 2H), 6.97 – 6.85 (m, 2H), 4.33 (s, 2H), 2.55 (s, 6H).

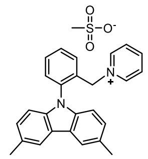

1-(2-(3,6-Dimethyl-9H-carbazol-9-yl)benzyl)pyridin-1-ium methanesulfonate (**5**) **KL1421**. (2-(3,6-Dimethyl-9H-carbazol-9-yl) phenyl)methanol (**4**) (0.15 g, 0.50 mmol, 1.0 equiv) was dissolved in anhydrous DCM (7.6 mL) and the solution was cooled to 0°C. MsCl (77.0 µL, 1.00 mmol, 2.0 equiv.) and DIPEA (0.40 mL, 2.00 mmol, 4.0 equiv.) were added to the solution and the obtained pale yellow solution was stirred at 0°C for 1 h. Then the reaction mixture was diluted with DCM (13 mL) and water (13 mL), the layers were separated and the organic layer was extracted with water (20 mL). The organic layer was dried over anhydrous Na_2SO_4 and concentrated under reduced pressure. The residue was dissolved in MeCN (2.5 mL) to give a clear, yellow solution. Pyridine (0.40 mL, 5.00 mmol, 10.0 equiv.) was added to the solution. The solution was stirred at room temperature. After 72 h the reaction mixture was diluted with Et_2O (50 mL), filtered under argon atmosphere. The precipitates were washed with Et_2O and recrystallized from MeCN/Et_2O to give product **5** as a white solid (162 mg, 70 %).

^{1}**H NMR** (300 MHz, MeOD) δ 8.04 – 7.93 (m, 2H), 7.93 – 7.86 (m, 2H), 7.87 – 7.73 (m, 4H), 7.62 – 7.46 (m, 1H), 7.43 – 7.28 (m, 2H), 7.19 – 7.06 (m, 2H), 6.73 – 6.63 (m, 2H), 5.56 (s, 2H), 2.68 (s, 3H), 2.51 (s, 6H).

2.3. *Characterization*

2.3.1. *Sample preparation*

The samples have been prepared and studied in powder form. Five milligrams of the powder have been selected for each experiment, described in sessions 2.3.2-2.3.4. For instance, the powder samples have been deposited into a sample holder with a cylindrical cavity of 0.7 cm in diameter and 0.5 mm in depth. Thin powder layers with homogeneous surfaces have been achieved. After adsorption tests and optical characterization, the powders were transferred into specific holders and vials for NMR, XRD, and FTIR measurements.

2.3.2. *Structure and optical properties*

The structure properties of the samples were studied by XRD (Bruker D8 diffractometer, CuKa radiation, Germany) and FTIR (ATR mode, Bruker II Alfa, Germany).

Optical properties of the luminophore have been studied by diffuse reflectance spectroscopy and photoluminescence in UV-Visible range. Ocean optics fiber optic light source (DH2000, 250-900 nm, USA), integrating sphere (Ocean optics, IS-8, USA) and fiber optic spectrometer (Ocean optics HR4000, USA) have been used to record diffuse reflectance spectra.

Excitation of photoluminescence and Quantum Yield of the photoluminescence have been measured by using FS5 spectrofluorometer (Edinburgh Instruments, Livingston, Scotland), equipped with plug-in integrating-sphere sample module SC-30 (150 mm internal sphere diameter). Three measurements have been performed to obtain average values of the excitation spectra and the Quantum Yield. Pyrene (QY of 30 %) was used as a reference compound to validate the measurements.

Photoluminescence of the luminophore has been excited by UV LED 325 nm. The excitation power of the LED varied from 0.068 mW to 0.6 mW.

Photoluminescence of the samples has been measured in steady state and kinetic modes. Full photoluminescence spectra (emission intensity vs wavelength) were obtained and analyzed against change of the photoluminescence intensity and peak position of the photoluminescence spectrum. Kinetic measurements have been performed as measurements of emission intensity at the fixed wavelength (483 nm) with time of the measurements. The stability of the signal (noise to signal ratio) has been evaluated from kinetic measurements as a ratio of standard deviation of the measured photoluminescence intensity to average value of the photoluminescence intensity during measurement time (1100 seconds).

2.3.3. *Adsorption tests*

The reaction of the KL1421 molecule with vapors of water (H_2O), ammonia (NH_3), and acetic acid (AcOH) was investigated using the photoluminescence method. The measurements have been performed at fixed excitation power (325 nm, 0.07 mW). Steady-state spectra of photoluminescence have been recorded before and after the adsorption of the vapor molecules. Kinetic measurements have been performed by recording the photoluminescence intensity at peak wavelength (483 nm) every 5 seconds.

Filter paper partially immersed in water, acetic acid, and 30 % ammonia solution, has been used as a source of vapors. The KL1421 sample and vapor source were placed in the same Petry dish. For each of the vapor probes the qualitative reaction of interaction between the luminophores and vapor molecules was measured. The vapor adsorption and desorption time remained at 10 minutes for each cycle.

2.3.4. *Fluorescence lifetime*

The single-spot measurement setup comprises a laser controller and a picosecond/cw laser (PicoQuant: 405 nm, pulse half-width 59 ps, repetition rate 20 MHz, mod. LDH-D-C-405) with 200-µm silica core optical fiber output via the SMA-connector. The excitation fiber represented one leg of a Y-shaped optical fiber bundle that contained an additional six fibers to deliver the fluorescent light via a monochromator to the photon counting detector (Becker&Hickl, HPM-100-07). The laser controller and photon counting detector were connected to a PC with a data processing card (Becker&Hickl, TCSPC, mod. SPC-150). The fiberoptic probe was tightly fixed such that the distance between the sample surface and the tip of the Y-shaped fiber bundle was 3 mm. The detection wavelength for fluorescence lifetime was 483 nm. Evaluation of lifetime has been performed by using Origin 2018 software in a mode of single exponential decay function.

3. Results

3.1. Theoretical calculations

The structure of the core molecule compound KL1421, with the addition of different guest molecules, was studied utilizing the generalized gradient approximation for the exchange-correlation potential in the density functional theory (DFT). The method is referred to as B3LYP and is described by Becke’s three-parameter hybrid functional together with the non-local correlation by Lee, Yang, and Parr [29–31]. The calculations were performed using the GAUSSIAN09 package [32] using the standard cc-pVTZ basis set.

Initially, the geometry of the KL1421 was optimized without any restraint using B3LYP/cc-pVTZ method. Next, the position of the mesylate counterion ($CH_3SO_3^-$) was explored. To this end, the counterion was placed in multiple positions around the pyridinium species, and the energies of the obtained luminophore structures were compared. The most energetically favored geometry was chosen for future studies (Fig. 2a).

With optimized luminophore geometry in hand, we proceeded with the exploration of the guest molecule’s influence on the properties of the luminophore. In order to locate the optimal positions of the guest molecules (ammonia, acetic acid, and water), ONIOM calculations [33] were used, taking into account the electronegativity of the “joined” elements. When the most probable positions of the guest molecules were found, the calculations were repeated using an *ab initio* method. In all cases, the introduction of the guest molecule resulted in slight changes in luminophore conformation and a shift of mesylate position, which is indicated by dipole momentum changes (Fig. 2b, Fig. 2c, Fig. 2d).

Our calculations show that adding the NH_3 molecule results in enlargement of the

Table 1
Frontier orbital energies of luminophore KL1421 and its complexes with guest molecules.

	KL1424	KL1424–H_2O	KL_1424–NH_3	KL_1424–AcOH
HOMO, eV	5.741	5.977	5.874	5.900
LUMO, eV	2.601	2.721	2.587	2.544
Δ, eV	3.139	3.256	3.286	3.356

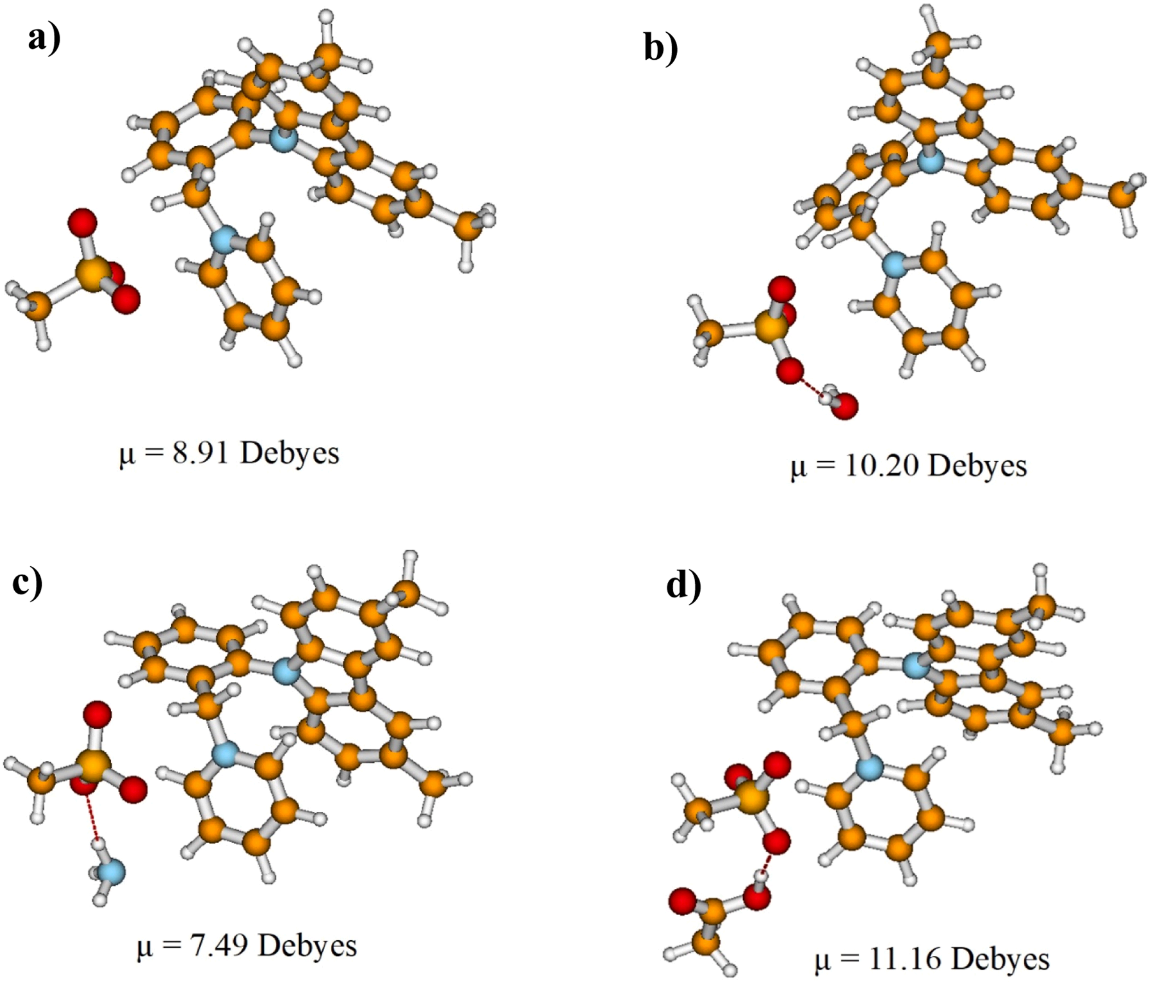

Fig. 2. Optimized geometries of the luminophore KL1421 pyridinium core and mesylate (**a**), KL1421–H_2O complex (**b**), KL1421–NH_3 complex (**c**), and KL1421–AcOH complex (**d**).

HOMO-LUMO gap (shown in Table 1). Specifically, the HOMO-LUMO gap for the KL1421 is 3.139 eV, while it increases slightly by 0.117 eV to 3.256 eV in the presence of water. A similar increase in the gap by 0.147 eV to 3.286 eV was predicted in the presence of the more basic ammonia. However, the largest increase of 0.217 eV to 3.356 eV was obtained for the complex of acetic acid and luminophore KL1421.

Fig. 3

In order to understand the electronic transitions of the luminophore and its complexes during the vertical excitation, the TD-DFT calculations were performed. The calculations revealed that the complexation of KL1421 with guest molecules resulted in the blueshift of the absorption spectrum (Table 2). The complexation of luminophore with both water and ammonia results in a significant blueshift of the lowest energy transition from 504.29 nm to 461.24 nm and 454.85 nm, respectively. Whereas this transition is slight in the case of acetic acid, which is from 504.29 nm to 475.27 nm.

Table 2

Vertical excitation modes of the luminophore KL1421 and its guest molecule complexes (triplets are excluded).

Entry	Excitation	Absorption wavelength, nm	Oscillator strength
KL1421			
1	HOMO to LUMO	504.29	0.0044
2	HOMO-1 to LUMO	455.17	0.0028
3	HOMO-2 to LUMO+2	397.70	0.0013
4	HOMO to LUMO+1	370.59	0.0002
KL1424–H_2O			
5	HOMO to LUMO	461.24	0.0014
6	HOMO-2 to LUMO	445.54	0.0010
7	HOMO-3 to LUMO	401.94	0.0015
8	HOMO-1 to LUMO+1	343.96	0.0026
KL1424–NH_3			
9	HOMO to LUMO	454.85	0.0028
10	HOMO-1 to LUMO	437.08	0.0027
11	HOMO-2 to LUMO	383.56	0.0014
12	HOMO-3 to LUMO	339.80	0.0004
KL1424–AcOH			
13	HOMO to LUMO	475.27	0.0012
14	HOMO-1 to LUMO	450.09	0.0000
15	HOMO-2 to LUMO	412.84	0.0017
16	HOMO to LUMO+1	358.45	0.0030

3.2. *Structure, optical, and sensor properties of KL1421 luminophore*

Chemical stability and structural properties of KL1421 before and after testing in different atmospheres have been studied by NMR, XRD, and FTIR spectroscopy. The ^{1}H NMR spectra of the samples before and after exposure to guest molecules were recorded using MeOD-d_4 as solvent and are shown in Fig. 4. The spectra of KL1421 (black line no 1) consists of 7 multiples in the aromatic region from 8.04 to 6.63 ppm. The singlet of the benzylic carbon is located at 5.56 ppm, while the singlet of the carbazole methyl substituents is located at 2.51 ppm. Meanwhile, the singlet of the methyl group of the mesylate counterion is located at 2.68 ppm. No noticeable changes in ^{1}H NMR were observed after the luminophore was exposed to the atmospheres of water vapors (red line no 2) and ammonia (green line no 3). Meanwhile, after exposure to an atmosphere containing acetic acid vapors, a new singlet located at 1.99 ppm was observed. This singlet corresponds to the methyl group of acetic acid. Additionally, a slight shift of the singlet of the methyl group of the mesylate counterion to 2.69 ppm was observed. The observations indicate that the acetic acid is absorbed on the surface of the KL1421, most likely through the formation of a hydrogen bond [34] with the mesylate counter ion.

XRD spectra of the KL1421 are shown in Fig. 5. As prepared KL1421 powders showed good crystallinity with intense peaks at 2θ positions: 6.78, 13.62 and 20.52° (Fig. 5a, curve 1). No significant changes have been observed after exposition of the KL1421 into H_2O and ammonia

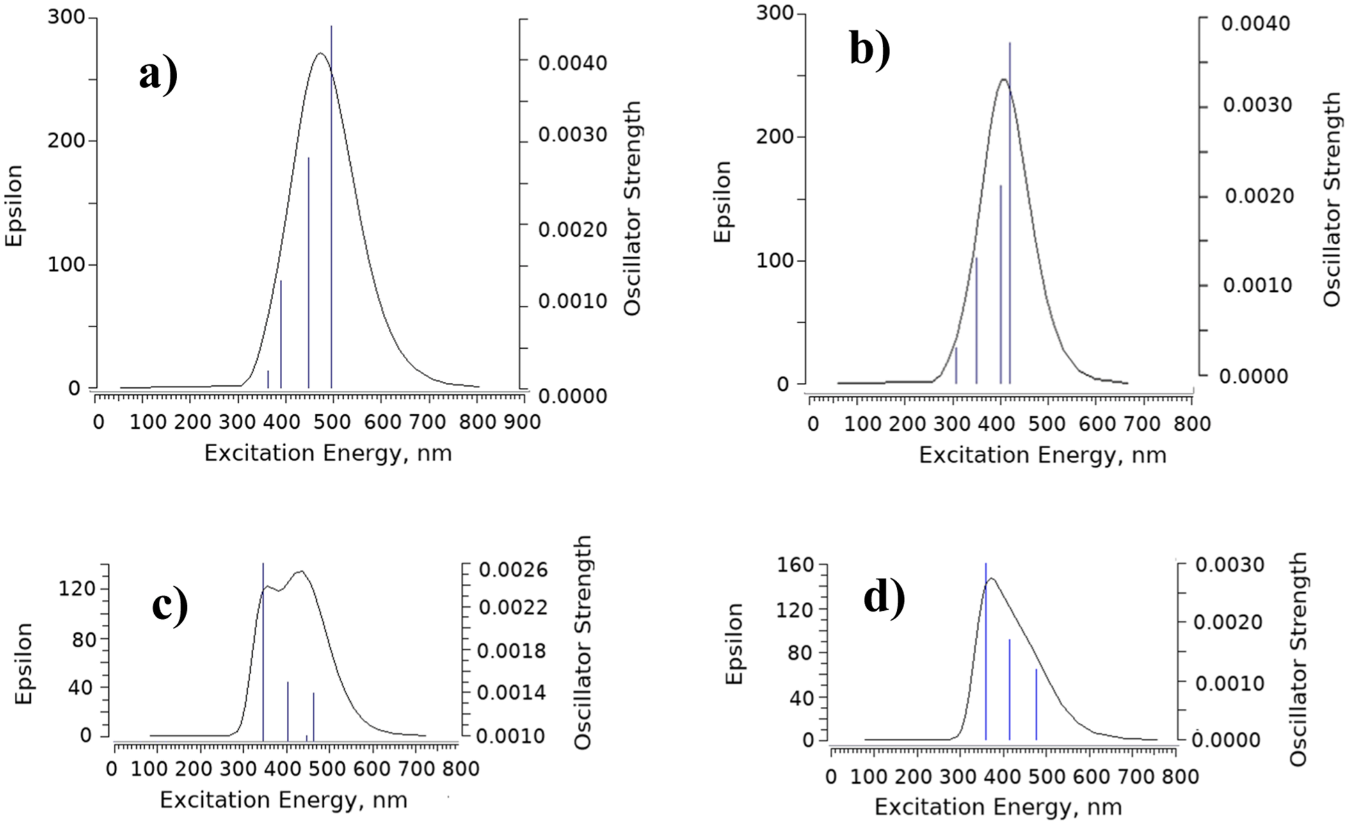

Fig. 3. Calculated spectra of absorption for (a) KL1421, (b) KL1421-NH_3[AK1], (c) KL1421-H_2O, (d) KL1421-AcOH. The blue bars correspond to single electronic transitions.

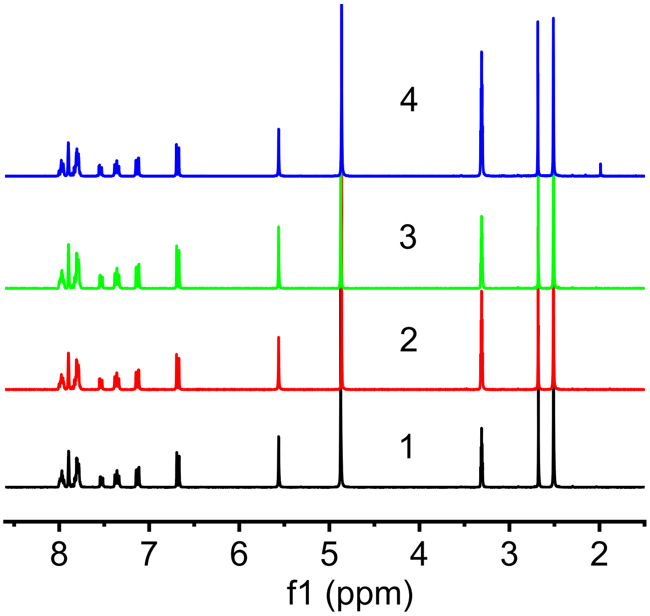

Fig. 4. ^{1}H NMR spectra of KL1421: 1- as prepared, 2- in water atmosphere, 3 - in ammonia atmosphere, 4 - acetic acid atmosphere.

atmospheres (Fig. 5a, curves 2,3). Based on the data reported in [11], we assume that KL1421 has triclinic structure. Using numerical simulations for triclinic crystalline structure and the lattice parameters data, reported in [11], we calculate (hkl) indexes of the planes with the following data (001), (002) and (030). Interaction of KL1421 with acetic acid resulted in the formation of two new peaks at 2θ positions 7.8 and 15.83° (Fig. 5a, curve 4). Comparison of the interplane distances with corresponding values of the triclinic crystalline lattice didn't give any of matching. We assume that the presence of new peaks suggests a phase transition of the KL1421 crystalline structure. Comparison of XRD data with ^{1}H NMR results points to interaction between acetic acid and mesylate ion, forming complexes within the luminophore's crystalline lattice.

FTIR spectra of the pyridinium luminophore before and after interaction with target molecules are shown in Fig. 5b. The following groups of peaks are observed in the FTIR spectra: 3500, 3200, 2900-2800, 1650-1600, 1500-1430, 1360-1300, 1221-1140, 1038 cm^{-1}. These peaks could be assigned to vibrations described in Table 3. The most important S=O stretching vibrations, characteristic of mesylate ion, typically appear in the 1100-1300 cm^{-1} region [35–37].

Interaction with ammonia and water didn't change the FTIR spectrum of the KL1421. On the other hand, the FTIR spectrum of the KL1421 after interaction with acetic acid showed significant changes (Fig. 5b, curve 4). New peaks at 3400 and 1719 cm^{-1}, related to O-H and C=O stretch vibrations, respectively, were observed. Moreover, the change of the peak shape at 1118 cm^{-1} can be attributed to hydrogen bonding interaction between the mesylate ion and acetic acid [38].

The mesylate anion ($CH_3SO_3^-$), being the conjugate base of methanesulfonic acid (CH_3SO_3H), can participate in proton transfer reactions and participate in hydrogen bonding in the presence of acetic acid [40]. Particularly, the mesylate ion can act as a base, accepting a proton from acetic acid to form methanesulfonic acid and the acetate ion or it can participate in hydrogen bonding with the carboxylic acid group of acetic acid. As the ^{1}H NMR spectra shows the presence of acetic acid, two new peaks were observed in XRD analysis, and FTIR analysis shows the presence of carboxylic groups and changes of S=O vibrations, we assume both mechanisms are possible.

Adsorption and interaction of molecules with KL1421 is expected to change HOMO-LUMO energies, as it was demonstrated in theoretical calculations. Diffuse reflectance spectroscopy is a method which can validate the way of interaction. Fig. 6a shows spectra of the diffuse reflectance measured before and after interaction with target molecules. The as-prepared samples show light scattering in the range of 450-800 nm, depicting a decrease of the reflectance value up to 60 % (Fig. 6a, curve 1). The absorption edge of the as-prepared KL1421 luminophore falls in the range 370-420 nm. This finding shows prospective optoelectronic applications of KL1421 in the UV-A-Vis range of the spectra. Interaction of KL1421 with water and ammonia doesn't drastically

Table 3
Vibrational modes in pyridinium-based luminophores.

Interaction	Absorption wavenumber, cm^{-1}	Possible interaction
1	3500	Broad peak from (methyl)pyridinium ion [39]
2	3000	Peaks from (methyl)pyridinium ion [39]
3	2900-2800	C-H (Sp3 hybridization) and C=C (Sp2 hybridization) [39]
4	1550-1300	Peaks from pyridinium ion and carbazole group [39]
5	1200 -1000	Peaks mostly from pyridinium ion and mesylate ion [39]

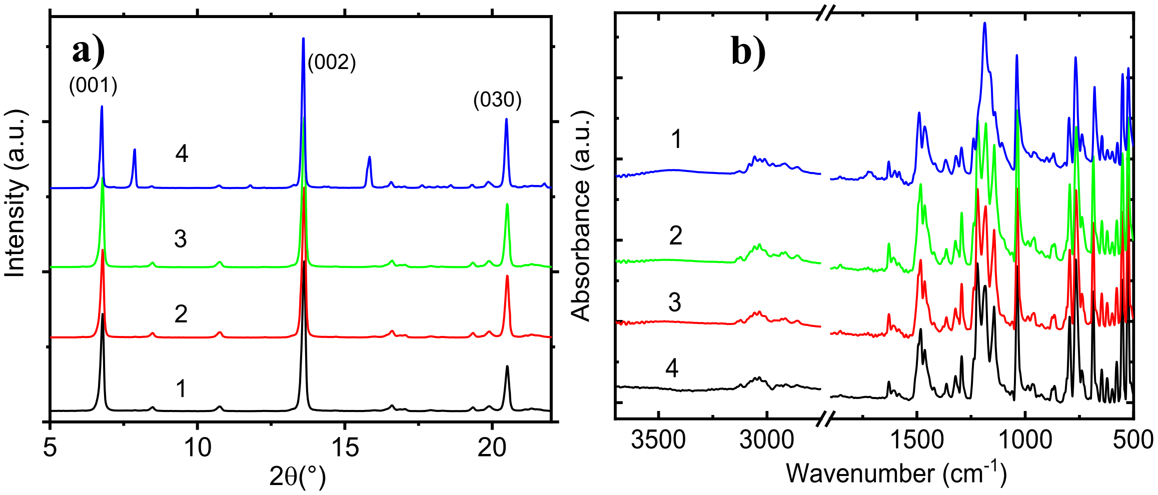

Fig. 5. Structure properties of the KL1421 luminophores: **a)** XRD spectra of as prepared KL1421 (1), after exposure to water (2), ammonia (3) and acetic acid (4); **b)** FTIR spectra of as prepared KL1421 (1), after exposure to water (2), ammonia (3) and acetic acid (4).

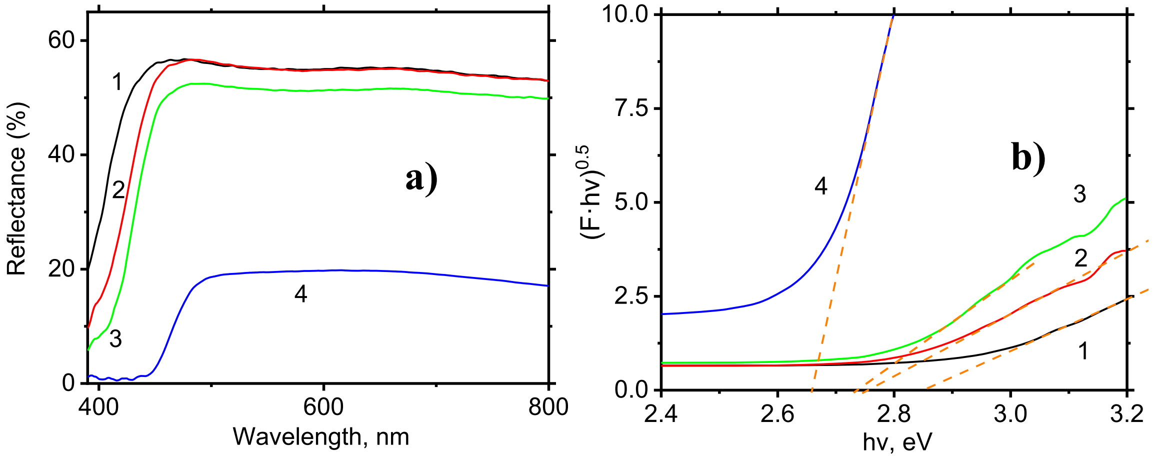

Fig. 6. UV-VIS optical properties of the KL1421 luminophores: **a)** diffuse reflectance of as prepared KL1421 (1), after exposure to water (2), ammonia (3) and acetic acid (4); **b)** band gap calculation of as prepared KL1421 (1), after exposure to water (2), ammonia (3) and acetic acid (4).

change the reflectance value in the range of 460-800 nm (Fig. 6a, curve 2,3). However, it results in red shift of the absorption edge for both target molecules. Interaction between KL1421 and acetic acid significantly changed the diffuse reflectance spectra (Fig. 6a, curve 4), demonstrating decrease of the reflectance value up to 20 % and the highest red shift of the absorption edge.

The observed results could be explained by type of interaction KL1421-target molecule. Hydrogen bonding and dipole-dipole interaction between the luminophore and water/ammonia lead to the change of HOMO-LUMO positions and reduction of the energy of the light, necessary for optical transition of the electron from the ground state to the excited state. The acetic acid interacting with KL1421 leads to chemical reaction and phase transitions resulting a change of the HOMO-LUMO positions, scattering/absorption and charge transfer mechanisms.

In order to evaluate the observed effect with theoretical calculations, we have estimated the optical band gaps of the studied luminophores. According to our previous work, the diffuse reflectance is converted to absorbance by using Kubelka-Munk equation:

$$F = \frac{(1-R)^2}{2 \cdot R} \qquad (1)$$

Where F is absorption coefficient and R is the diffuse reflectance. The optical transitions can be described by the Tauc's equation:

$$(F \cdot h\nu)^n = A \cdot (h\nu - E_g) \qquad (2)$$

Where hν, n, A and E_g are photon energy, power coefficient (n=1/2 or 2 for indirect and direct optical transitions, respectively), constant and band gap energy, correspondently. We have plotted the equation (2) for n=2 and n=0.5. The linear approximation has been found only for n=0.5 (Fig. 6b). The band gap values have been graphically calculated and the obtained data was summarized in the Table 4.

Table 4
Band gap data of the KL1421 before and after interaction with target molecules.

Target molecule	Band gap, eV	Equivalent wavelength (1240/$h\nu$(eV), nm)	Theoretical HOMO-LUMO transitions, nm
KL1421 as prepared	2.85	435	504
KL1421-H_2O	2.75	451	461
KL1421-NH_3	2.7	459	454
KL1421-Acetic acid	2.66	466	475

Analysis of the band gap values and theoretical calculations showed significant difference in HOMO-LUMO transitions for as prepared KL1421 luminophore. The calculations showed good correlation between HOMO1-LUMO (455 nm) and the experimental band gap. The theoretical calculations of HOMO-LUMO transitions for KL1421 in different atmospheres showed error of 10 nm. The deviations in calculations could be explained by simple mode of the calculations, based on modelling of one KL1421 molecule in a gas phase. The developed calculations don't take in account the interaction between KL1421 molecules in the crystalline lattice. The hydrogen bonding and non-covalent interaction result in red shift of the HOMO-LUMO transition energies, what correlates well with experimental data. The model doesn't assume chemical interaction between mesylate ions and acetic acid. As this is first approach for modelling of interaction between new Py-type luminophores and volatile compounds, the proposed model will be improved in our future works.

Photoluminescence spectroscopy is one of the powerful methods for investigation interaction of organic luminophores with target molecules and understanding internal mechanisms of charge transfer.

In order to evaluate the optimal excitation efficiency, an excitation spectrum of the KL1421 photoluminescence have been investigated (Fig. 7a). The efficient excitation of the PL falls in the range of 310-415 nm. This finding shows good compatibility of the KL1421 with low-cost LEDs with a center wavelength in the range of 365-405 nm. Deconvolution of the PL spectrum on separate peaks showed four peaks at 466, 499, 544, and 605 nm (Fig. 7b). The emission lines, obtained from deconvolution, are significantly different from the absorption line of HOMO-LUMO transitions, presented in Table 2. The difference between absorption and emission could be explained by the thermal relaxation of excited electrons.

The effect of the excitation wavelength and excitation power on photoluminescence intensity has been investigated at room temperature (Fig. S1a). The peak intensity dependence on the excitation power had linear dependence (Fig. S1b). This linear dependence of the emission intensity vs excitation power could be useful for optoelectronic applications of the KL1421.

As reported before, one of the main advantages of pyridinium luminophores is high quantum yield (QY), which is a key factor for possible optoelectronic applications of these materials [11]. Based on aggregation-induced emission, the developed KL1421 luminophores showed a significantly high QY of 80 % (Fig. 8a).

The QY value of the KL1421 has insignificantly decreased under exposure to water and ammonia atmospheres. Meanwhile, the interaction of the KL1421 and acetic acid led to a decrease of the QY value to 35 %. It has been shown that the QY strongly depends on intermolecular

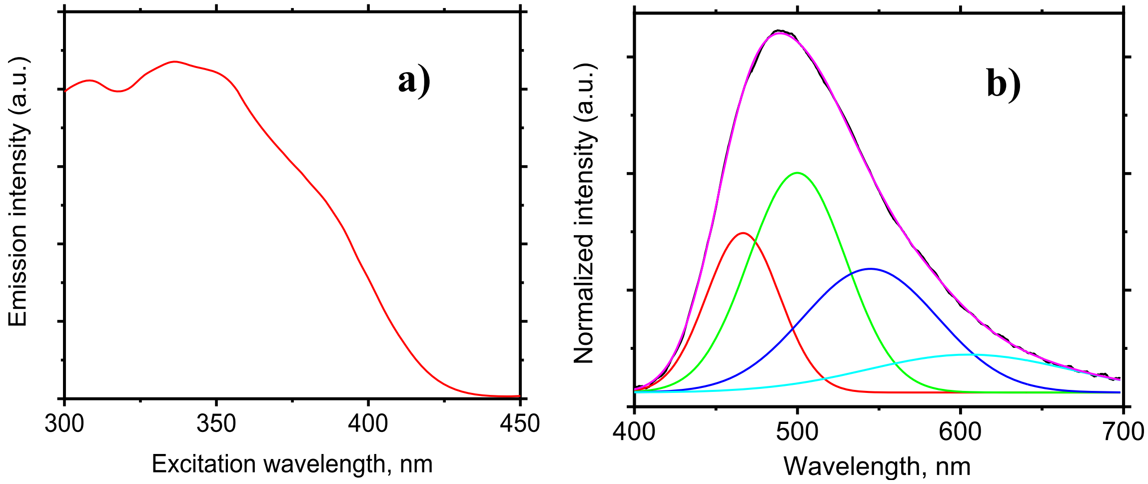

Fig. 7. Photoluminescence properties of the KL1421 luminophores: **a)** excitation spectrum; **b)** deconvolution of photoluminescence spectrum in single peaks (black curve is experimental spectrum and purple curve is the sum of deconvoluted peaks).

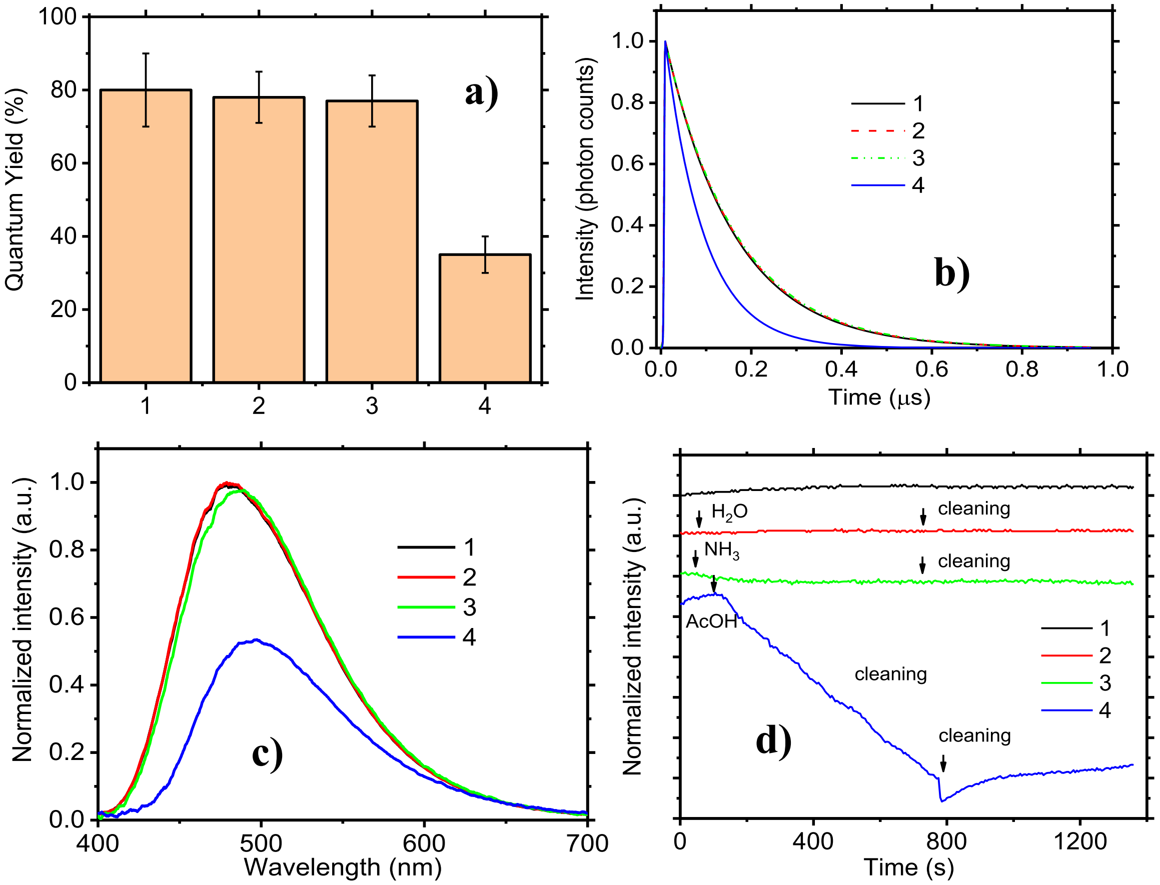

Fig. 8. Photoluminescence properties of the KL1421 luminophores: **a)** quantum Yield measurements of as prepared KL1421 (1), after exposure to water (2), ammonia (3) and acetic acid (4); **b)** photoluminescence lifetime measurements of as prepared KL1421 (1), after exposure to water (2), ammonia (3) and acetic acid (4); **c)** photoluminescence measurements of as prepared KL1421 (1), after exposure to water (2), ammonia (3) and acetic acid (4); **d)** photoluminescence kinetics measurements of as prepared KL1421 (1), sensor response to water (2), ammonia (3) and acetic acid (4).

charge transfer between the luminophore molecules [11]. Therefore, the small change of the QY in water and ammonia atmospheres is a good indication that the possible hydrogen bonding and non-covalent interactions are transient and do not influence structural properties of the luminophore. On the other hand, the drastic change of the QY after exposure to the acetic acid confirms our previous assumption that acetic acid provokes changes in the crystal structure of the luminophore and influences the charge transfer properties of KL1421.

The photoluminescence lifetime decay curves are plotted in Fig. 8b. We have found no significant changes in the photoluminescence decay curve of KL1421 before and after the adsorption of water and ammonia. Meanwhile, the interaction with acetic acid resulted in a faster decay of the photoluminescence signal. The calculated values of photoluminescence lifetime (Supplementary information Fig. S2a,b) are summarized in Table 4. We conclude that an interaction with acetic acid resulted in a decrease in lifetime from 157 ns to 86 ns. The change in the lifetime value is one of the proofs of the change in the charge transfer mechanism for KL1421. We assume that photogenerated electrons are transferred to the excited states of the newly formed luminophore-acetic acid complexes and undergo non-radiative transitions to the ground state.

The KL1421 photoluminescence spectra before and after adsorption of target molecules are presented in Fig. 8c. The KL1421 photoluminescence spectrum didn't change after water adsorption. The photoluminescence intensity of KL1421 insignificantly decreased due to interaction with ammonia. A slight peak shift of the KL1421 photoluminescence spectrum was observed after ammonia adsorption. The interaction of KL1421 with acetic acid led to drastic decrease of photoluminescence intensity (over 60 % of signal change) and a strong red shift of the peak position (18 nm). The results, presented in Fig. 8c are in good correlation with QY measurements.

Table 5

The stability of the photoluminescence signal of KL1421 and its interaction with target molecules have been studied by using photoluminescence spectroscopy in kinetic measurement mode (Fig. 8d). The kinetic measurements of as deposited KL1421 showed stability of the photoluminescence intensity during measurement time with noise to signal ratio 3 % (Fig. 8c, curve 1). Similarly to steady state measurements of the photoluminescence, the kinetic curve of the KL1421 photoluminescence showed no changes before and after water adsorption.

The kinetic test of KL1421 response to ammonia is presented in Fig. 8d (curve 3). The photoluminescence intensity value decreased due to interaction with ammonia. Cleaning of the measurement chamber by air flow didn't result in the signal recovery.

Interaction of KL1421 with acetic acid was recorded during 700 seconds. The photoluminescence signal has not reached saturation. The cleaning of the chamber by air didn't lead to the recovery of the luminescence signal. The kinetic measurements show that water, ammonia and acetic acid remain into KL1421 physically adsorbed forming weak hydrogen bonds (water and ammonia) and strong chemical bonds (acetic acid).

The reaction time, high concentration of the tested vapors and changes in photoluminescence properties of the KL1421show quite good stability of the KL1421 in humid and basic environment opposite to acidic environment where strong interaction observed.

The sensor response to acetic acid doesn't fulfill the general sensor requirement about fast reaction time and signal saturation.

Investigation of optical properties of the KL1421 in different atmospheres showed that combining diffuse reflectance and photoluminescence spectroscopy, we were able to monitor the interaction between KL1421 and volatile compounds. Despite weak interaction in water and ammonia leading to a change of HOMO-LUMO transition energy and red shift of absorption edge, photoluminescence of the KL1421 showed quite high stability, low noise-to-signal ratio, and high quantum yield. From our results, we assume that dual-mode measurements of photoluminescence and diffuse reflectance could be used for monitoring of chemical composition of the environment. Based on high quantum yield values, encapsulation of KL1421 into a polymeric matrix is a prospective application for new luminophores as passive optical coatings for environmental safety monitoring.

Table 5
The fluorescence lifetime, measured at 483 nm.

Sample name	Lifetime, ns
KL1421	157±2ns
KL1421-H_2O	155±2ns
KL1421-NH_3	156±2ns
KL1421-Acetic Acid	86±2ns

In the present stage, the use of dual-mode detection of changes in optical properties of the KL1421 enables the detection of a leakage of volatile acids in the environment. These findings open future prospects for investigation of novel pyridinium luminophore-based optical sensors for environmental applications. We are currently working on the improvement of the sensor properties of the KL1421 towards volatile acids, such as HCl, TFA, and formic acid, by tuning the chemical structure of the KL1421.

In the present work, theoretical calculations showed significant deviation from experimental results in the prediction of the fundamental properties of novel pyridinium luminophores. Based on important applications and prospects of the novel materials, we consider that the improved theoretical design and modelling of structure, optical, and sensor properties of pyridinium luminophores will stimulate faster and efficient development of novel luminophores for advanced applications.

4. Conclusions

We have investigated the influence of volatile gases on the optical properties of the high quantum yield pyridinium luminophore KL1421. From theoretical calculations, based on the B3LYP method using a standard cc-pVTZ basis set, energies of the HOMO-LUMO gap, absorption spectra, and oscillatory strengths of the luminophore complexes with guest molecules – water, ammonia, and acetic acid were obtained.

Characterization of structural properties of the luminophore was performed using ^{1}H NMR, XRD, and FTIR methods. The luminophores preserved chemical structure after exposure to water and ammonia environment; however, after exposure to acetic acid vapors, phase transition of the crystalline structure was observed. The change could be attributed to the formation of a complex due to interaction between acetic acid and the mesylate anion of the luminophore.

The theoretical calculations showed possible hydrogen bonding also with water and ammonia; however, these proved to be transient and did not result in structural changes of the luminophore. The calculations also predict the formation of a hydrogen bond between the mesylate anion of the luminophore and acetic acid; indeed, acetic acid, as a strong hydrogen bond donor, promoted changes in crystallinity of the luminophore, as evidenced by XRD and FTIR, however not predicted by theoretical calculations.

Optical properties of the KL1421 have been measured by UV-VIS and photoluminescence spectroscopy. Red shift of the absorption edge has been observed after exposure of KL1421 to water and ammonia vapors. Meanwhile, a significant red shift of the absorption edge and a decrease in the diffuse reflectance were found after exposure of KL1421 to acetic acid vapors. The band gaps of KL1421 in different environments were calculated and compared with HOMO-LUMO transition energies. Theoretical calculations showed small deviations from experimental values of the band gaps for KL1421, exposed to water, ammonia, and acetic acid vapors. The theoretical calculations of HOMO-LUMO and band gap for KL1421 showed a difference of 0.4 eV. On the other hand, the calculated value HOMO1-LUMO of KL1421 fits well with the obtained band gap 2.85 eV). We conclude that the modelling of the luminophore properties should be improved in future works, taking into account the crystalline structure and corresponding interactions in the theoretical model.

Unmodified KL1421 showed a high quantum yield (80 %). The quantum yield of KL1421 in water and ammonia didn't significantly change, whereas the quantum yield dropped to 35 % in acetic acid vapors. Interaction of KL1421 with water showed no changes in photoluminescence properties, whereas interaction with ammonia and acetic acid led to an irreversible decrease of intensity and red shift of the photoluminescence peak position. Photoluminescence lifetime studies showed a decrease in the lifetime value from 154 ns to 87 ns in acetic acid vapors.

On the basis of theoretical and experimental results, we conclude that the interaction of KL1421 with water and ammonia results in transient hydrogen bonds formation which doesn't change the charge transfer mechanism responsible for the photoluminescence. On the other hand, exposure of KL1421 to acetic acid vapors results in the formation of strong hydrogen bonds and adsorption of the acetic acid on the luminophore, which promotes structural changes resulting in a change in charge transfer mechanism.

The developed pyridinium luminophores have good prospects in sensor development for environmental applications. As prepared KL1421 luminophore showed a good signal stability, low noise-to-signal ratio of the photoluminescence signal and linear dependence of photoluminescence intensity vs excitation power. The presence of water and ammonia can be detected by dual mode measurements by combining diffuse reflectance and photoluminescence. The KL1421 has future prospects as advanced photoluminescence coating for applications in environment with high humidity and pH. We envision that the KL1421 could be integrated in advance coatings and thin films or polymer matrix and used for volatile acid sensor design using excitation with low-cost LED (wavelength 365-405 nm). Improvements to KL1421 sensitivity and selectivity towards volatile acids will be studied in our future work.

CRediT authorship contribution statement

Viktor Zabolotnii: Writing – original draft, Methodology, Investigation, Data curation. **Jelena Tamuliene:** Writing – original draft, Visualization, Validation, Software, Funding acquisition, Formal analysis, Data curation, Conceptualization. **Matiss Martins Drava:** Writing – original draft, Visualization, Methodology, Investigation, Data curation. **Teodora Kirova:** Writing – original draft, Software, Investigation, Data curation. **Iryna Tepliakova:** Writing – original draft, Visualization, Investigation, Formal analysis, Data curation. **Vanesa Lukinsone:** Writing – original draft, Visualization, Methodology, Formal analysis, Data curation, Conceptualization. **Artis Kinens:** Writing – original draft, Visualization, Validation, Supervision, Methodology, Funding acquisition, Formal analysis, Data curation, Conceptualization. **Roman Viter:** Writing – original draft, Validation, Supervision, Resources, Project administration, Funding acquisition, Formal analysis, Data curation, Conceptualization.

Declaration of competing interest

The authors declare that they have no known competing financial interests or personal relationships that could have appeared to influence the work reported in this paper.

Acknowledgements

Numerical calculations with GAUSSIAN09 package were performed at the High-Performance Computing Center of Vilnius University "HPC Sauletekis". Experimental work has been performed with support of the project: "Piridīnija luminofora strukturālo un optisko īpašību projektēšana pielāgotai sensora reakcijai", Nr. LU-BA-PA-2024/1-0040

Supplementary materials

Supplementary material associated with this article can be found, in the online version, at doi:10.1016/j.apmt.2025.102890.

Data availability

Data will be made available on request.

References

[1] Z. Wu, H. Choi, Z.M. Hudson, Achieving white-light emission using organic persistent room temperature phosphorescence, Angew. Chem. Int. Ed. 62 (2023) e202301186, https://doi.org/10.1002/ANIE.202301186.

[2] E. Amador, G. Belev, A.R. Kalapala, J. Mohapatra, Y. Wei, N. Pandey, R. Sammynaiken, J.P. Liu, W. Zhou, W. Chen, A new pyridinium-substituted tetraphenylethylene aggregation induced emission composites for rare-earth free white light displays, Mater. Today Phys. 33 (2023) 101036, https://doi.org/10.1016/J.MTPHYS.2023.101036.

[3] K. Wu, Y. Zheng, R. Chen, Z. Zhou, S. Liu, Y. Shen, Y. Zhang, Advances in electrochemiluminescence luminophores based on small organic molecules for biosensing, Biosens. Bioelectron. 223 (2023) 115031, https://doi.org/10.1016/J.BIOS.2022.115031.

[4] S. Mukherjee, P. Thilagar, Recent advances in purely organic phosphorescent materials, Chem. Commun. 51 (2015) 10988–11003, https://doi.org/10.1039/C5CC03114A.

[5] K. Leduskrasts, E. Suna, Aggregation induced emission by pyridinium–pyridinium interactions, RSC Adv. 9 (2018) 460–465, https://doi.org/10.1039/C8RA08771G.

[6] K. Leduskrasts, A. Kinens, E. Suna, Cation–π interactions secure aggregation induced emission of planar organic luminophores, Chem. Commun. 55 (2019) 12663–12666, https://doi.org/10.1039/C9CC06829E.

[7] K. Zhang, J. Liu, Y. Zhang, J. Fan, C.K. Wang, L. Lin, Theoretical study of the mechanism of aggregation-caused quenching in near-infrared thermally activated delayed fluorescence molecules: hydrogen-bond effect, J. Phys. Chem. C (2019) 123, https://doi.org/10.1021/ACS.JPCC.9B06388/SUPPL_FILE/JP9B06388_SI_001.PDF.

[8] S. Yamada, Cation–π interactions in organic crystals, Coord. Chem. Rev. 415 (2020) 213301, https://doi.org/10.1016/J.CCR.2020.213301.

[9] K. Leduskrasts, E. Suna, Aggregation induced emission in one easy step: pyridinium AIEgens and counter ion effect, RSC Adv. 10 (2020) 38107–38113, https://doi.org/10.1039/D0RA07137D.

[10] K. Leduskrasts, E. Suna, Intermolecular charge-transfer luminescence by self-assembly of pyridinium luminophores in solutions, ChemistryOpen 10 (2021) 1081–1086, https://doi.org/10.1002/OPEN.202100191.

[11] K. Leduskrasts, A. Kinens, E. Suna, The emission efficiency of cationic solid state luminophores is directly proportional to the intermolecular charge transfer intensity, Chem. Commun. 59 (2023) 6905–6908, https://doi.org/10.1039/D3CC01674A.

[12] J. Morse, N. Ofodum, F.K. Tang, M. Schmidt, X. Lu, K. Leung, Leveraging Metal Complexes for Microsecond Lifetime-Based Chloride Sensing, ACS Sens, 2025, https://doi.org/10.1021/ACSSENSORS.4C03195/SUPPL_FILE/SE4C03195_SI_001.PDF.

[13] S. Rana, S. Vaidyanathan, S. Patel, Aggregation induced emission (AIE) based donor–π–acceptor fluorophores: an approach to fabricate acidochromic sensors and white light emitting diodes, J. Mater. Chem. C Mater. 12 (2024) 14148–14164, https://doi.org/10.1039/D4TC02617A.

[14] J.V.S. Medeiros, A.P.T. Padilha, K.A. da Silva, A.H. de Oliveira, V.F. da Silva, R. M. Araújo, R.C. Balaban, R. Cristiano, M.A.F. de Souza, F.G. Menezes, Experimental and theoretical study of the photochemical properties and acidochromism of nonconventional 2,4,6-triarylpyridine-based materials, Dyes Pigm. 230 (2024) 112361, https://doi.org/10.1016/J.DYEPIG.2024.112361.

[15] A.S. Manna, S. Ghosh, T. Ghosh, N. Karchaudhuri, S. Das, A. Roy, D.K. Maiti, Smart luminescent materials for emerging sensors: fundamentals and advances, Chem. Asian J. 20 (2025) e202401328, https://doi.org/10.1002/ASIA.202401328.

[16] Z.F. Lutfi, D.S. Ahmed, N.M. Hussien, Y.M. Mohialden, I.S. Mohammed, N. J. Mousa, Design and implementation of an emergency environmental monitoring system, Electronics 14 (2025) (2025) 287, https://doi.org/10.3390/ELECTRONICS14020287. Page 287 14.

[17] L. Ji, J. Shi, J. Wei, T. Yu, W. Huang, L. Ji, J. Shi, J. Wei, T. Yu, W. Huang, Air-Stable organic radicals: new-generation materials for flexible electronics? Adv. Mater. 32 (2020) 1908015 https://doi.org/10.1002/ADMA.201908015.

[18] E.K. Lee, M.Y. Lee, C.H. Park, H.R. Lee, J.H. Oh, Toward environmentally robust organic electronics: approaches and applications, Adv. Mater. 29 (2017) 1703638, https://doi.org/10.1002/ADMA.201703638.

[19] M. Turemis, D. Zappi, M.T. Giardi, G. Basile, A. Ramanaviciene, A. Kapralovs, A. Ramanavicius, R. Viter, ZnO/polyaniline composite based photoluminescence sensor for the determination of acetic acid vapor, Talanta 211 (2020) 120658, https://doi.org/10.1016/J.TALANTA.2019.120658.

[20] R. Viter, A. Abou Chaaya, I. Iatsunskyi, G. Nowaczyk, K. Kovalevskis, D. Erts, P. Miele, V. Smyntyna, M. Bechelany, Tuning of ZnO 1D nanostructures by atomic layer deposition and electrospinning for optical gas sensor applications, Nanotechnology 26 (2015) 105501, https://doi.org/10.1088/0957-4484/26/10/105501.

[21] R. Rega, A. Fioravanti, F. Borbone, M. Mazzocchi, S. Lettieri, Oxygen sensing without organic molecules: Mixed-phase TiO2 as cost-effective ultrasensitive optical sensors, Sens. Actuators B Chem. 433 (2025) 137560, https://doi.org/10.1016/J.SNB.2025.137560.

[22] L.M. Sikhwivhilu, S. Mpelane, B.W. Mwakikunga, S.Sinha Ray, Photoluminescence and hydrogen gas-sensing properties of titanium dioxide nanostructures synthesized by hydrothermal treatments, ACS Appl. Mater. Interfaces 4 (2012) 1656–1665, https://doi.org/10.1021/AM2018089/ASSET/IMAGES/MEDIUM/AM-2011-018089_0010.GIF.

[23] C. Mercado, Z. Seeley, A. Bandyopadhyay, S. Bose, J.L. McHale, Photoluminescence of dense nanocrystalline titanium dioxide thin films: Effect of doping and thickness and relation to gas sensing, ACS Appl. Mater. Interfaces 3

(2011) 2281–2288, https://doi.org/10.1021/AM2006433/SUPPL_FILE/AM2006433_SI_001.PDF.

[24] D.D. La, S.V. Bhosale, L.A. Jones, S.V. Bhosale, Tetraphenylethylene-Based AIE-active probes for sensing applications, ACS Appl. Mater Interfaces 10 (2018) 12189–12216, https://doi.org/10.1021/ACSAMI.7B12320/ASSET/IMAGES/MEDIUM/AM-2017-123203_0039.GIF.

[25] A.B. Kajjam, D.K. Dubey, R.A. Kumar Yadav, J.H. Jou, V. Sivakumar, Tetraphenylimidazole-based luminophores for explosive chemosensors and OLEDs: experimental and theoretical investigation, Mater. Today Chem. 14 (2019) 100201, https://doi.org/10.1016/J.MTCHEM.2019.100201.

[26] É. Brémond, A. Ottochian, Á.J. Pérez-Jiménez, I. Ciofini, G. Scalmani, M.J. Frisch, J.C. Sancho-García, C. Adamo, Assessing challenging intra- and inter-molecular charge-transfer excitations energies with double-hybrid density functionals, J. Comput. Chem. 42 (2021) 970–981, https://doi.org/10.1002/JCC.26517.

[27] A. Mazarevics, A. Kinens, K. Leduskrasts, E. Suna, Tailoring emission lifetime for dopant-induced phosphorescence, ACS Mater. Lett. (2024) 4590–4595, https://doi.org/10.1021/ACSMATERIALSLETT.4C01412/SUPPL_FILE/TZ4C01412_SI_006.CIF.

[28] P. Ulukan, E. Lognon, S. Catak, A. Monari, Intersystem crossing in a dibenzofuran-based room temperature phosphorescent luminophore investigated by non-adiabatic dynamics, Phys. Chem. Chem. Phys. 26 (2024) 22261–22268, https://doi.org/10.1039/D4CP02474E.

[29] A.D. Becke, Density-functional thermochemistry. III. The role of exact exchange, J. Chem. Phys. 98 (1993) 5648–5652, https://doi.org/10.1063/1.464913.

[30] A.D. Becke, Density-functional thermochemistry. I. The effect of the exchange-only gradient correction, J. Chem. Phys. 96 (1992) 2155–2160, https://doi.org/10.1063/1.462066.

[31] A.D. Becke, Density-functional thermochemistry. II. The effect of the Perdew–Wang generalized-gradient correlation correction, J. Chem. Phys. 97 (1992) 9173–9177, https://doi.org/10.1063/1.463343.

[32] M.J.; T.G.W.; S.H.B.; S.G.E.; R.M.A.; C.J.R.; S.G.; B.V.; P.G.A., Frisch, Gaussian 09, Revis. A.02, Wallingford, Gaussian, Inc., CT, USA, 2016.

[33] T. Vreven, K. Morokuma, Chapter 3 hybrid methods: ONIOM(QM:MM) and QM/MM, Annu. Rep. Comput. Chem. 2 (2006) 35–51, https://doi.org/10.1016/S1574-1400(06)02003-2.

[34] M. Zhang, L. Chen, H. Yang, J. Ma, Theoretical Study of Acetic Acid Association Based on Hydrogen Bonding Mechanism, J. Phys. Chem. A 121 (2017) 4560–4568, https://doi.org/10.1021/ACS.JPCA.7B03324/ASSET/IMAGES/MEDIUM/JP-2017-03324K_0014.GIF.

[35] S.F. Parker, E.J. Revill-Hivet, D.W. Nye, M.J. Gutmann, Structure and vibrational spectroscopy of lithium and potassium methanesulfonates, R Soc. Open Sci. 7 (2020), https://doi.org/10.1098/RSOS.200776.

[36] A. Chihab, N. El Brahmi, E. Kazzouli, S. Synthesis, N. Saghdani, A. Chihab, N. El Brahmi, S. El Kazzouli, Synthesis and characterization of novel indazole–sulfonamide compounds with potential MAPK1 inhibitory activity for cancer treatment, Molbank 2024 (2024), https://doi.org/10.3390/M1858. Page M1858 2024 (2024) M1858.

[37] K.C. Schreiber, Infrared spectra of sulfones and related compounds, Anal. Chem. 21 (1949) 1168–1172, https://doi.org/10.1021/AC60034A005/ASSET/AC60034A005.FP.PNG_V03.

[38] L. Pu, Y. Sun, Z. Zhang, Hydrogen bonding of hydrates of double acetic acid molecules, J. Phys. Chem. A 113 (2009) 6841–6848, https://doi.org/10.1021/JP902634H/SUPPL_FILE/JP902634H_SI_001.PDF.

[39] M. Akçay, FT-IR spectroscopic investigation of the adsorption pyridine on the raw sepiolite and Fe-pillared sepiolite from anatolia, J. Mol. Struct. 694 (2004) 21–26, https://doi.org/10.1016/J.MOLSTRUC.2004.01.010.

[40] A. Telfah, Z. Charifi, N. latelli, I.A. Qattan, H. Baaziz, Q.M. Al-Bataineh, A. M. Alsaad, R.F. Sabirianov, Formation of hydrogen bonding network of methane sulfonic acid at low degree of hydration (MSA)m·(H2O)n (m = 1–2 and n = 1–5), Nature.ComA Telfah, Z Charifi, N Latelli, IA Qattan, H Baaziz, QM Al-Bataineh, AM Alsaad, RF SabirianovScientific Reports 14 (2024) (2024), https://doi.org/10.1038/S41598-024-61364-0 nature.Com.